

# Limits on the luminosity function of Ly $\alpha$ emitters at $z = 7.7$ $\star$

P. Hibon<sup>1,2</sup>, J.-G. Cuby<sup>1</sup>, J. Willis<sup>4</sup>, B. Clément<sup>1</sup>, C. Lidman<sup>3</sup>, S. Arnouts<sup>5,1</sup>, J.-P. Kneib<sup>1</sup>, C. J. Willott<sup>6</sup>, C. Marmo<sup>7</sup>, and H. McCracken<sup>7</sup>

<sup>1</sup> Laboratoire d'Astrophysique de Marseille, OAMP, Université Aix-Marseille & CNRS, 38 rue Frédéric Joliot Curie, 13388 Marseille cedex 13, France

<sup>2</sup> Korean Institute for Advanced Study, Dongdaemun-gu, Seoul 130-722, Korea

<sup>3</sup> European Southern Observatory, Alonso de Cordova 3107, Vitacura, Casilla 19001, Santiago 19, Chile

<sup>4</sup> Department of Physics and Astronomy, University of Victoria, Elliot Building, 3800 Finnerty Road, Victoria, BC, V8P 1A1, Canada

<sup>5</sup> Canada France Hawaii Telescope Corporation, Kamuela, HI 96743, USA

<sup>6</sup> Herzberg Institute of Astrophysics, National Research Council, 5071 West Saanich Rd, Victoria, BC V9E 2E7, Canada

<sup>7</sup> Institut d'Astrophysique de Paris, Université Pierre et Marie Curie, 98bis boulevard d'Arago, 75014 Paris, France

## ABSTRACT

**Aims.** The Ly $\alpha$  luminosity function (LF) of high-redshift Ly $\alpha$  emitters (LAEs) is one of the few observables of the re-ionization epoch accessible to date with 8-10 m class telescopes. The evolution with redshift allows one to constrain the evolution of LAEs and their role in re-ionizing the Universe at the end of the Dark Ages.

**Methods.** We have performed a narrow-band imaging program at 1.06  $\mu\text{m}$  at the CFHT, targeting Ly $\alpha$  emitters at redshift  $z \sim 7.7$  in the CFHT-LS D1 field. From these observations we have derived a photometric sample of 7 LAE candidates at  $z \sim 7.7$ .

**Results.** We derive luminosity functions for the full sample of seven objects and for sub-samples of four objects. If the brightest objects in our sample are real, we infer a luminosity function which would be difficult to reconcile with previous work at lower redshift. More definitive conclusions will require spectroscopic confirmation.

**Key words.** cosmology: early Universe - galaxies: luminosity function, mass function - galaxies: high-redshift

## 1. Introduction

Searching for high-redshift galaxies is one of the most active fields in observational cosmology. The most distant galaxies provide a direct probe of the early stages of galaxy formation in addition to revealing the effects of cosmic re-ionization (Fan et al. 2006). Galaxies at redshift 6 are routinely found and show that star formation was initiated at significantly higher redshifts and that these galaxies are the likely sources of the re-ionization of the universe which was completed at this redshift. Conversely, detection of  $z > 7$  galaxies is still rare, due in large part to the complete absorption of their restframe UV emission below the Ly $\alpha$  line which is redshifted beyond the 1  $\mu\text{m}$  cutoff wavelength of silicon. The deployment of large format IR arrays at many telescopes now makes these observations possible. From  $z = 6.5$  to  $z = 7.7$  light dimming due to luminosity distance is 30% and the age of the Universe varies by 150 Myr, leading to a further dimming, probably moderate considering the relatively short time span, of the galaxy intrinsic luminosities. Observations of  $z > 7$  objects should therefore remain within

reach of the current generation of telescopes. However, at  $z > 6.5$  the Universe is thought to be undergoing re-ionization and this may cause a further evolution of the observable properties of very distant objects with redshift, possibly more abrupt than their intrinsic evolution and dimming with age and distance.

One prime tracer of high-redshift galaxies is the Ly $\alpha$  line. The determination of the Ly $\alpha$  Luminosity Function (LF) with infrared arrays is actively pursued by several groups, either through narrow-band imaging (e.g Willis et al. 2008; Cuby et al. 2007), or through blind spectroscopy along the critical lines of galaxy clusters used as gravitational telescopes (Richard et al. 2006; Stark et al. 2007; Bouwens et al. 2008). High- $z$  galaxies are also searched using the dropout technique between the optical and near infrared domains, either in the field (see e.g. Bouwens et al. 2009) or behind galaxy clusters (see e.g. Richard et al. 2008). The dropout method is primarily sensitive to the UV continuum emission of the galaxies and therefore allows to determine their UV Luminosity Function (UVLF).

The UVLF of LAEs is a direct tracer of galaxy evolution and it is not affected by the amount of neutral hydrogen in the intergalactic medium (IGM), while the Ly $\alpha$  emission (and therefore the Ly $\alpha$  LF) may be affected. A rapid change in the ionization state of the Universe could lead to a decline of the Ly $\alpha$  luminosity density at high-redshift, while the UVLF should have a milder evolution. Evidence for such a rapid change of the neutral fraction of the Intergalactic Medium between redshifts 6 and 7 includes the observation of LAEs in narrow-band imaging at  $z = 6.5$  (Kashikawa et al. 2006) and at  $z = 7$  (Ota et al. 2008) and in spectroscopy at  $z > 7$  (Richard et al. 2008). The patchy structure of a partially ionized Universe should also affect the

Send offprint requests to: P. Hibon

$\star$  Based on observations obtained at the Canada-France-Hawaii Telescope (CFHT) which is operated by the National Research Council (NRC) of Canada, the Institut National des Sciences de l'Univers of the Centre National de la Recherche Scientifique of France (CNRS), and the University of Hawaii. This work is based in part on observations obtained with MegaPrime/MegaCam, a joint project of CFHT and CEA/DAPNIA and in part on data products produced at TERAPIX and the Canadian Astronomy Data Centre as part of the Canada-France-Hawaii Telescope Legacy Survey, a collaborative project of NRC and CNRS.

apparent clustering of LAEs at high redshifts, see Mesinger & Furlanetto (2008) for an analysis of this effect at  $z \sim 9$ .

More observations of LAEs at high redshifts are necessary to better characterize the re-ionization epoch, and in particular observations in the near-IR domain to probe redshifts  $\geq 7$ . Willis & Courbin (2005), Willis et al. (2008) and Cuby et al. (2007) have performed narrow-band surveys at  $z = 8.8$  which have yielded only upper limits of the Ly $\alpha$  LF of LAEs at this redshift. In this paper we present the results of a narrow-band imaging survey at  $z = 7.7$  representing a factor of 10 improvement in area at approximately the same detection limit compared to our previous survey at  $z = 8.8$ . These observations were made with the Wide Field near-IR Camera (WIRCam) operating at CFHT<sup>1</sup>.

In section 2, we describe the narrow-band observations and other observational material used in this paper. In section 3, we discuss the construction of our sample of Ly $\alpha$  emitters. In section 4, we infer from this sample an estimate of the Ly $\alpha$  luminosity function of  $z = 7.7$  LAEs and discuss it in the light of existing models.

Unless explicitly stated otherwise, we use AB magnitudes throughout the paper. We assume a flat  $\Lambda$ CDM model with  $\Omega_M = 0.27$  and  $H = 70 \text{ km s}^{-1} \text{ Mpc}^{-1}$ .

## 2. Observational data

The CFHT-LS D1 field was chosen for the availability of multi-wavelength data from the X ray to the near-IR, including in particular extremely deep optical data from the CFHT-LS survey. For the purpose of this study, we originally made use of the so-called T0004 release of the CFHT-LS survey, and later of the T0005 release when it became available (November 2008). The CFHT-LS data products are available from the CADC archive to CFHT users and consist in various image stacks in the  $u^* g' r' i' z'$  filters and of ancillary data, such as weight maps, quality checks, catalogs, etc. The  $u^*, g', r', i', z'$  filters have spectral curves similar to the SDSS filters.

The core data relevant to this paper are deep near-IR Narrow Band (NB) observations of a  $\sim 20' \times 20'$  area of the CFHT-LS D1 Deep Field, totalling  $\sim 40$  hrs of integration time. In addition to the narrow-band near-IR data we made use of broad band  $J, H$  and  $K_s$  data of the field which were acquired as part of another program carried out with WIRCam (PIs Willott & Kneib). We also used near-IR Spitzer/IRAC data from the SWIRE survey (Lonsdale et al. 2003).

A summary of the observational data used in this paper is provided in table 1. Figure 1 shows the transmission curves of the filters corresponding to the multi-band data used in this paper.

### 2.1. WIRCam narrow-band data

WIRCam is a  $\sim 20' \times 20'$  imager installed at the CFHT prime focus. It is equipped with 4 Hawaii2-RG arrays, the pixel scale is  $0.3'' \text{ pixel}^{-1}$  and the four arrays are separated by a  $\sim 15''$  gap. We used a Narrow Band filter centered at  $1.06 \mu\text{m}$  (hereafter referred to as NB1060) with a full width at half maximum of  $0.01 \mu\text{m}$  ( $\sim 1\%$ ). This filter was designed to match a region of low night sky OH emission.

The data were acquired in service mode over several months in two different semesters in 2005 and 2006, each epoch totalling approximately the same integration time ( $\sim 20$  hrs). A detector

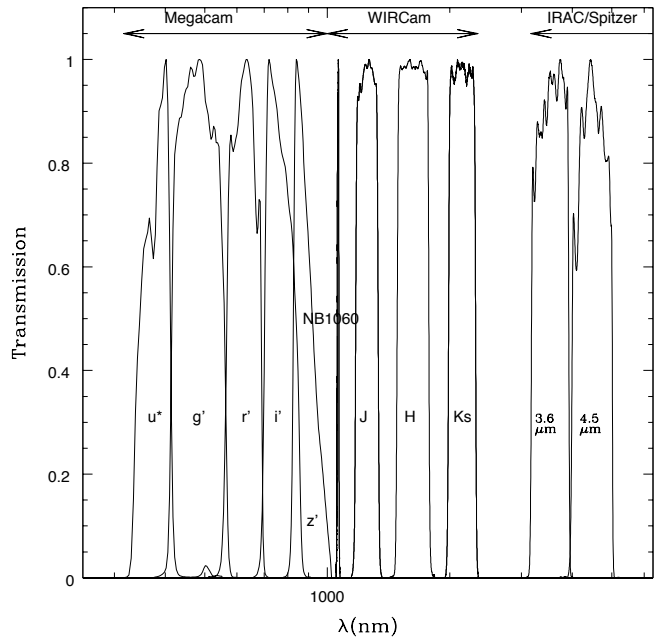


**Fig. 1.** Transmission curves of the filters corresponding to the data used in this paper. All transmissions are normalized to 100% at maximum.

integration time of 630 s was used, ensuring background limited performance. The sky background was measured to be of the order of  $4 \text{ e}^- \text{ s}^{-1} \text{ pixel}^{-1}$  which corresponds to a sky brightness of  $\sim 17.7 \text{ mag arcsec}^{-2}$  (Vega). Our first observations started shortly after the commissioning of the camera. The detector was experiencing variable readout noise and significant electronic crosstalk, both issues that were progressively solved in the subsequent months of operations. The first year data were the most affected. We discuss in a subsequent section of this paper the effects of the electronic cross-talk as a possible source of contamination.

With WIRCam the only possibility to guide the telescope is through the on-chip guiding capability implemented in the detector controller. This is achieved by clocking adequately small detector windows around bright stars for fast readout and rapid guiding. This feature does also leave some residuals on the images along the detector lines where the windows are located.

The narrow-band data were pre-processed at CFHT (dark subtraction and flat fielding). The pre-processed images were then stacked together at the Terapix data processing center at Institut d'Astrophysique de Paris (IAP). The data reduction steps include double pass sky subtraction, astrometric and photometric calibration and final stacking of the images. Two separate stacks were produced for each of the one-year datasets. For the details of the data reduction, see Marmo (2007). We further combined these two stacks into a single stack corresponding to the entire dataset. After stacking, the useful area of the array after removal of the edges was  $390 \text{ arcmin}^2$ . The FWHM image quality of the final stacked image, as measured on stars, is  $\sim 0.76''$ .

### 2.2. WIRCam Broad band data

The broad band  $J$  and  $K_s$  WIRCam data were acquired in 2006 and 2007 and were processed similarly to the narrow-band data. We also had moderately deep SOFI (ESO-NTT)  $J$  and  $K_s$  band

<sup>1</sup> See <http://www.cfht.hawaii.edu/Instruments/Imaging/WIRCam/>

images covering one quarter of the WIRCam field (Iovino et al. 2005). This allowed us to improve the limiting magnitude by  $\sim 0.3$  mag in each of the  $J$  and  $Ks$  bands for the corresponding quadrant. We did not attempt at making use of the UKIDSS Deep Extragalactic Survey (UKIDSS-DXS) (Lawrence et al. 2007)  $J$ ,  $H$  and  $Ks$  images as these data are of significantly shallower depths. The image quality achieved in the  $J$  and  $Ks$  image is comparable to that of the  $NB1060$  image.

We note that the  $NB1060$  and  $J$  WIRCam filters do not overlap. The wavelengths of the blue and red ends of the full width at half maximum of the  $J$  filter are 1175 and 1333 nm. The  $J$  filter can therefore be used to trace the UV continuum above the Ly $\alpha$  line without being contaminated by line emission.

### 2.3. Photometric calibration

Due to the general lack of photometric calibration data in narrow-band filters and to the lack of systematic observations of standard stars with the WIRCam  $NB1060$  filter, we performed the photometric calibration of the narrow-band dataset using stars present in the field. For consistency we used identical procedures for the photometric calibration of the entire MegaCam and WIRCam datasets. We initially selected stars on morphological criteria from the list of detected objects. We then selected those stars which were not saturated in any of our images. From this list of objects we finally kept those present in the 2MASS catalog. This led to a final stellar sample of 75 objects. We first determined the zero points of the WIRCam Broad Band data ( $J$  and  $Ks$ ) by minimizing the difference between the WIRCam and 2MASS magnitudes of the stellar sample. This left residuals of 0.07 and 0.15 magnitudes (rms) in the  $J$  and  $Ks$  bands respectively.

For the MegaCam data, we applied zero point offsets up to 0.06 magnitude to the photometric catalog distributed as part of the T0004 CFHT-LS release. These offsets were determined by Ilbert et al. (2006) when trying to adjust, for the purpose of determining photometric redshifts, the original CFHT-LS photometry to synthetic colors of galaxies derived from SED models. These offsets were originally determined for the T0003 release, and we used slightly modified ones corresponding to the T0004 release (Coupon et al. 2008; Ilbert et al. 2006).

As a parallel investigation, we generated synthetic colors for the MegaCam and WIRCam filters of a variety of stellar spectra models of various temperatures and metallicities (Marigo et al. (2008) and <http://stev.oapd.inaf.it/~lgirardi/cgi-bin/cmd>). While the WIRCam  $J$  and  $Ks$  magnitudes of the stellar sample did match well to the synthetic color tracks, the CFHT-LS magnitudes had to be slightly modified by offsets very similar to those mentioned above to better match the color tracks. This suggests that there are systematic offsets between the CFHT-LS photometry and synthetic colors of stars and galaxies. That the offsets for stars and galaxies are similar is not surprising for synthetic SED modeling of galaxies makes direct use of stellar spectra. More interesting is the fact that these offsets do not seem to depend on the models being used, as noted by Ilbert et al. (2006), a fact which seems re-inforced by our analysis since we used completely different synthetic stellar libraries.

Finally, we performed a last check using the stellar library of Pickles (Pickles 1998). This library consists of observed stellar spectra in the optical domain and in parts of the near-IR domain, with interpolations in between. Here again the color tracks derived for the MegaCam filters from this library do match the color tracks of our stellar sample after applying the same offsets as above.

From the color tracks we determined that the stars of the stellar sample used for the calibration have spectral types from G to M5. Then, from the calibrated  $u^*$ ,  $g'$ ,  $r'$ ,  $i'$ ,  $z'$ ,  $J$  and  $Ks$  data, we performed an ad hoc polynomial fitting of the fluxes of all objects in the stellar sample, from which we derived for each star the  $NB1060$  magnitude at  $1.06 \mu\text{m}$ . This simple method is justified in view of the large number of photometric datapoints (7) available, of the smooth spectral energy distribution of stars, and of the absence of features at the wavelength of the  $NB1060$  filter in the infrared spectra of stars of spectral types earlier than M5.

With the stellar  $NB1060$  magnitudes, we could then determine the zero points of our  $NB1060$  image. Because quadrants have slightly different gains, this was done separately for each quadrant. The rms residuals after this last step were 0.04 magnitude.

Making provision for additional sources of errors, e.g. the accuracy of the 2MASS photometry, possible biases from the selected sample of stars, etc., we estimate our final photometric accuracy to be of the order of 0.1 magnitude rms and we adopt this value in the rest of this paper.

### 2.4. Catalog generation and detection limits

We used SExtractor (Bertin & Arnouts 1996) in single image mode for object detection and photometry of the  $NB1060$  and Broad Band WIRCam images. The magnitudes were computed in apertures 5 pixels ( $1.5''$ ) in diameter. We used the CFHT-LS public images of the field for the optical  $u^*g'r'i'z'$  bands, photometrically corrected as explained in the previous section.

The limiting magnitude of the  $NB1060$ ,  $J$  and  $Ks$  WIRCam observations was estimated as follows: we added 200 artificial star-like objects per bin of 0.1 mag on the stacked  $NB1060$  image in carefully selected blank regions of the image. We then ran SExtractor on this image using the same parameters as previously used for object detection. Counting the number of artificial stars retrieved in each magnitude bin provided a direct measure of our completeness limit. We report in this paper the limiting magnitude at the 50% completeness limit.

In the optical we re-binned the original CFHT-LS images with  $0.19'' \text{ pixel}^{-1}$  images to the  $0.3'' \text{ pixel}^{-1}$  scale of the WIRCam images. We then ran SExtractor with the same parameters used with the WIRCam data. We checked that the photometry before and after re-binning was preserved. We then derived the completeness limit at 50% for the CFHT-LS images using the same methodology as described above for the WIRCam images.

In order to estimate the signal to noise ratio ( $SNR$ ) of our candidates and the  $SNR$  corresponding to our 50% completeness limit we used the noise image (BACKGROUND\_RMS) produced by SExtractor. This image gives for each pixel the local noise  $\sigma$ . The  $SNR$  of an object with number of counts  $F$  in an aperture of  $A$  pixels is given by:

$$SNR = F / \sqrt{A\sigma^2} \quad (1)$$

and the error on the magnitude  $m$  by:

$$\Delta m = 1.086 / SNR \quad (2)$$

Finally, the limiting magnitude reached by the  $NB1060$  observations is 25.2 in apertures  $1.5''$  in diameter at the 50% completeness limit. This limit corresponds to a  $SNR$  of  $\sim 4$  and, converted into a pure emission line flux, to  $8.3 \times 10^{-18} \text{ ergs s}^{-1} \text{ cm}^{-2}$ .

The same procedure was used to derive the limiting magnitudes of all CFHT-LS and WIRCam images. They are reported in table 1.

**Table 1.** Observational data.

Instrument	Band	Integration time (hrs)	Limiting magnitude <sup>a</sup>
MegaCam	$u^*$	20.7	27.9
MegaCam	$g'$	25	28.1
MegaCam	$r'$	49	27.8
MegaCam	$i'$	74	27.4
MegaCam	$z'$	55.8	26.5
WIRCam	NB 1st epoch	20	24.8
WIRCam	NB 2nd epoch	20	24.9
WIRCam	NB combined	40	25.2
WIRCam	$J$	6.2	25.0 <sup>b</sup>
WIRCam	$H$	7.7	24.7
WIRCam	$Ks$	8.9	24.7 <sup>b</sup>
IRAC	$3.6 \mu\text{m}$	0.034	22.2
IRAC	$4.5 \mu\text{m}$	0.034	21.5

<sup>a</sup>  $4\sigma$  magnitude limits in apertures  $1.5''$  in diameter for MegaCam and WIRCam. These limits correspond to a 50% completeness level. IRAC limiting magnitudes are  $5\sigma$  in  $3.8''$  apertures.

<sup>b</sup> In one quarter of the field, for which additional NTT/SOFI data were available, magnitude limits of 25.2 in  $J$  and 24.8 in  $Ks$  were achieved.

### 3. Sample construction

#### 3.1. Initial candidate selection

We started by matching all catalogs corresponding to individual images to the  $NB1060$  catalog using a matching radius between positions of  $0.7''$  to allow for astrometric errors.

Our initial selection of Ly $\alpha$  candidates was based on the following criteria:

1. We selected objects detected in the  $NB1060$  image which do not have counterpart in any of the optical images ( $u^*$ ,  $g'$ ,  $r'$ ,  $i'$ ,  $z'$ ), as it is indeed virtually impossible to detect any flux blueward of the Ly $\alpha$  line. Negligible amounts of radiation are expected to escape the galaxy and to be transmitted by the IGM below the  $z = 7.7$  Lyman limit at  $\sim 790$  nm, and therefore to be detected in the  $u^*$ ,  $g'$  and  $r'$  bands. All the radiation between the Ly $\alpha$  and Ly $\beta$  lines at  $z = 7.7$  is entirely redshifted beyond the Gunn-Peterson (GP) trough at  $\sim 850$  nm observed in the spectra of high-redshift quasars (Fan et al. 2006), and which corresponds to Ly $\alpha$  absorption by the partially neutral IGM above  $z \sim 6$ . There should therefore be no detectable flux in the  $z'$  band. Moreover, all photons redder than the Lyman limit at  $z = 7.7$  are redshifted above the Ly $\beta$  and the Ly $\alpha$  troughs at  $z = 6$ , with therefore an optical depth of 5 or more (Fan et al. 2006) leading to very strong color breaks  $i' - J \gtrsim 5$  or more.
2. We required that the  $NB1060$  objects detected in the combined image be also detected in each of the half  $NB1060$  stacks corresponding to each epoch. While each half-stack is at lower  $SNR$  than the total combined image used for generating the master  $NB1060$  catalog, this criterion allows one to remove variable (in flux or in position) objects and reduces considerably the number of low  $SNR$  detections.
3. We required a signal to noise ratio of  $\sim 5$  or higher on the combined image, corresponding to a  $SNR \gtrsim 3.5$  in half stack images.

Considering the limiting magnitude of our optical and NB images, the selection criterion 1 above corresponds to:

$$\begin{aligned} u^* - NB1060 &> 2.7 \\ g' - NB1060 &> 2.9 \\ r' - NB1060 &> 2.6 \\ i' - NB1060 &> 2.2 \\ z' - NB1060 &> 1.3 \end{aligned} \quad (3)$$

Taken altogether, the color break between the optical and  $NB1060$  filters is extremely high and covers a wide spectral range. For the CFHT-LS, the Terapix data center generated deep  $\chi^2$  images combining the  $g'$ ,  $r'$  and  $i'$  images. Without entering into considerations on wide band / multi-color magnitudes, we can infer from equations 3 that the optical dropout selection can be broadly expressed as:

$$g' r' i' - NB1060 \gtrsim 3 \quad (4)$$

We note that this color break is significantly stronger than what has been usually achieved in other high- $z$  LAEs or LBGs searches, however with a slight gap in wavelength between the optical red end and the  $NB1060$  filter.

After this initial criterion, a careful visual inspection of the candidates allowed us to remove a few obvious fake candidates in the form of electronic ghosts or artifacts around bright stars. A couple of objects of dubious quality in one or some of the images, or with unusual morphology, were also removed.

Finally, three initial candidates that were bright in the  $Ks$  band image with  $NB1060 - Ks \gtrsim 1.2$  were interpreted as Extremely Red Objects (EROs) (see also section 3.3.6) and were therefore discarded, corresponding de facto to using an additional color selection criterion for the candidates:

$$NB1060 - Ks \lesssim 1.2 \quad (5)$$

From these simple criteria we derived an initial list of 8 objects, none of them being resolved at the level of the image quality of the  $NB1060$  image ( $0.76''$ ).

Finally, we note that none of the objects in our list do have counterparts in any of the Spitzer/IRAC SWIRE data. If the H $\alpha$  line was  $\sim 100$  times brighter than the Ly $\alpha$  line, it would still be too faint to be detected alone in the  $5.8 \mu\text{m}$  IRAC band to the sensitivity achieved by the SWIRE data.

#### 3.2. The sample

Our sample consists of 8 objects listed in table 2 and shown in Fig. 2. One has  $NB1060 - J \sim 0$  and therefore does *not* qualify as an emission line object, and is instead identified as a T-dwarf candidate (see section 3.3.5). Only 5 objects have  $NB1060 - J < 0$  and therefore qualify, a priori, as emission line objects, while two other objects have  $NB1060$  fluxes fainter than the detection limit in  $J$ , and therefore cannot be surely identified as line emitting objects. Therefore, from the six brightest objects of the original sample of eight selected without using the  $J$  magnitudes, five seem to be line emitters. With the same success rate of 5/6 the two faintest objects should therefore also be line emitters and it is therefore reasonable to keep them in the final sample, however flagging them as less secure than the other candidates.

We also report in table 2 the lower limits of the restframe Equivalent Widths ( $EW$ ) derived from the photometric data, defined as:

$$EW_{\text{rest}} = \left( \frac{f_{\lambda, \text{NB1060}} \times \lambda_{\text{NB1060}}^2}{f_{\lambda, J} \times \lambda_J^2} - 0.5 \right) \times \frac{\Delta \lambda_{\text{NB1060}}}{1+z} \quad (6)$$

where  $f_{\lambda}$  is the observed flux density in  $\text{ergs s}^{-1} \text{cm}^{-2} \text{\AA}^{-1}$  at the wavelengths of the NB1060 and  $J$  filters and  $\Delta \lambda_{\text{NB1060}}$  is the width of the NB1060 filter (100  $\text{\AA}$ ). It is assumed that the UV continuum is completely extinguished below the Ly $\alpha$  line, and therefore contributes to the NB1060 flux, in average, over only half of the filter spectral width. A spectral energy distribution  $f_{\nu} = \text{const.}$  is assumed. Assuming  $f_{\lambda} = \text{const.}$  would lead to  $EW$  values approximately twice as large. Six out of seven of our LAE photometric candidates are not detected in the  $J$  band and we therefore use the detection limit in this band, deriving in turn lower limit  $EW$  values. We note that LAE#6 and LAE#7 have positive  $EW$  values despite the fact that their NB1060 magnitudes are fainter than their  $J$  magnitudes.

Samples of emission line selected galaxies are nominally defined in terms of the limited equivalent width sampled by a particular survey. For example, Taniguchi et al. (2005) present a sample of 9 spectroscopically confirmed LAEs at  $z = 6.5$  with  $EW_{\text{obs}} > 130 \text{\AA}$  or  $EW_{\text{rest}} > 17 \text{\AA}$ . Of our sample of candidate  $z = 7.7$  LAEs, the faintest certain line emitters (e.g. LAE#5) presents  $\text{NB1060} - J < -0.3$  which corresponds to an  $EW$  limit  $EW_{\text{obs}} > 80 \text{\AA}$  or  $EW_{\text{rest}} > 9 \text{\AA}$ . Considering that in all but one case all the  $EW$  values are lower limits, the lower range of  $EW$ s sampled by our observations is comparable to that of other studies. Within the practical limitation of matching the selection criteria of two different surveys, the two populations of LAEs revealed by Taniguchi et al. (2005) and the current study are therefore approximately equivalent in terms of the  $EW$  sampled.

However, the  $z = 7.7$  LAEs presented in this paper are selected to be NB1060 excess sources at a lower significance level than the Taniguchi et al. (2005) LAEs, and in addition our sources are not confirmed spectroscopically. Therefore, when comparing the LF properties of the  $z = 7.7$  LAE candidates to confirmed LAE sources at  $z = 6.5$  we must include an assessment of the unknown sample contamination.

### 3.3. Possible sources of contamination

Known astronomical objects such as extremely red objects or T-dwarfs can potentially satisfy the optical dropout selection and therefore possibly contaminate our sample. We examine various such examples in this section, along with artificial sources of contamination.

In the discussion which follows we will make use of figure 3 which shows the NB1060 –  $K_s$  versus NB1060 –  $J$  colors of the candidates together with other astrophysical objects.

We used the template spectra (without emission lines) described in Ilbert et al. (2009). We then arbitrarily redshifted them in the redshift range [0–8] and we added arbitrary reddening values  $E(B - V)$  in the range [0–5], generating in total more than 100,000 spectra. We then applied our selection criteria (equation 3), computing for the remaining spectra the NB1060 –  $J$  and NB1060 –  $K_s$  colors. The envelope of the points corresponding to galaxies at redshifts  $< 6$  (respectively  $> 6$ ) is indicated by the dark (resp. light) grey zone in figure 3.

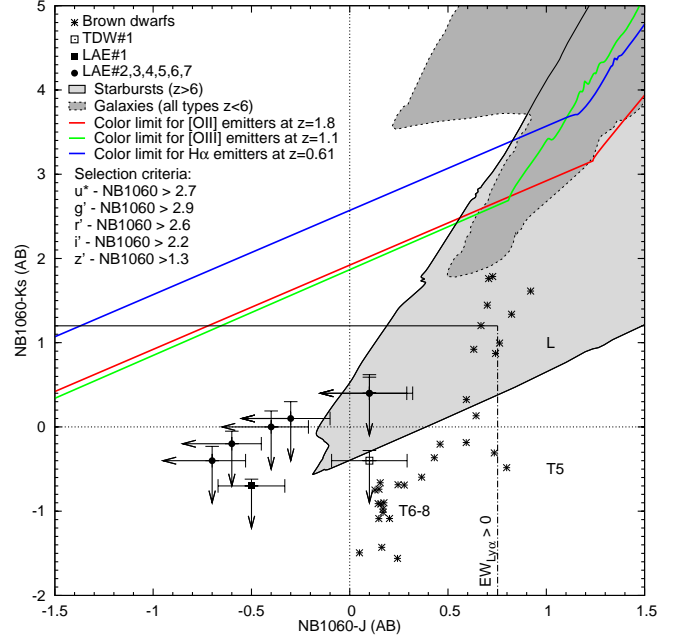


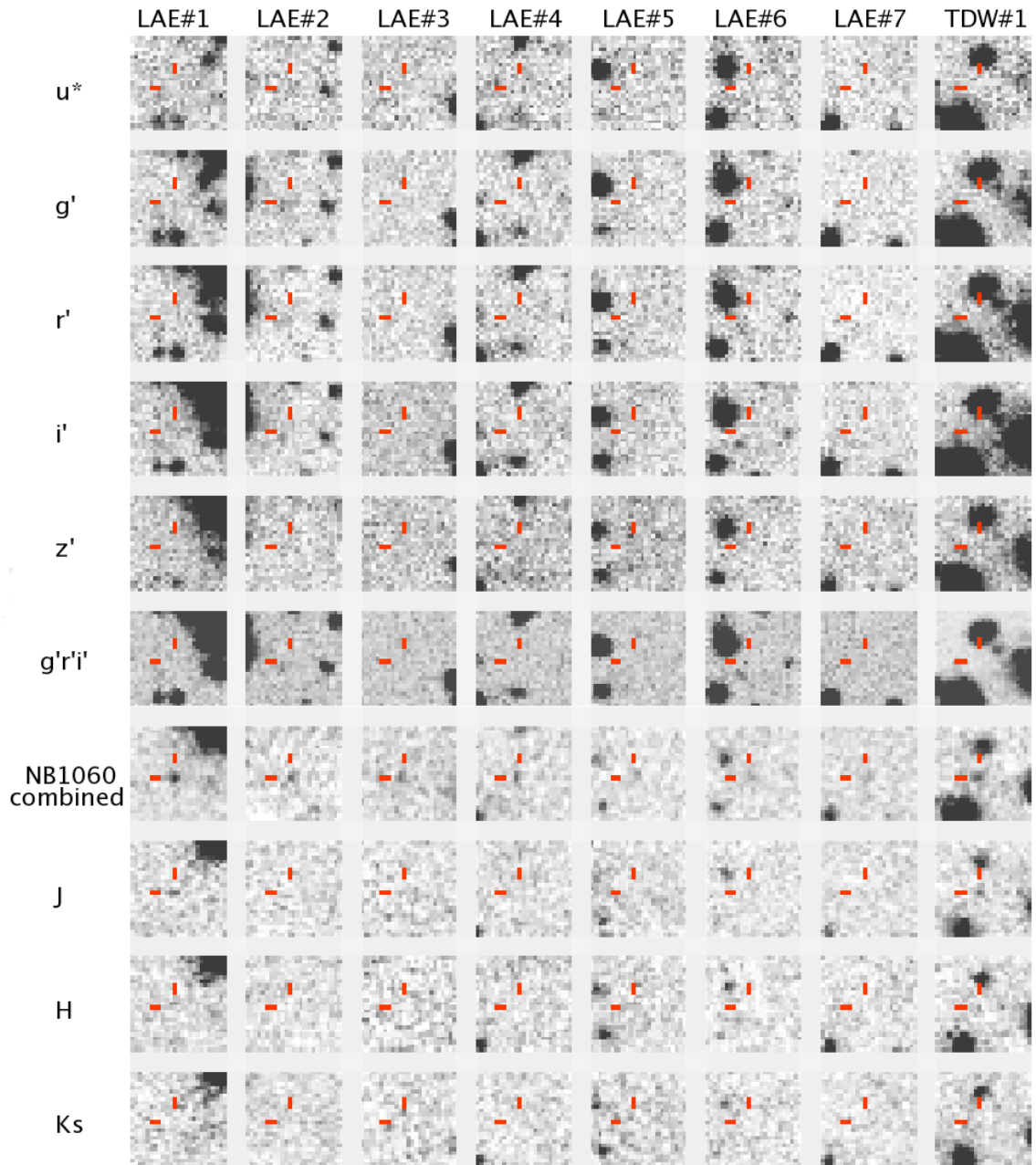
**Fig. 3.** NB1060 –  $J$  and NB1060 –  $K_s$  color-color diagram. The filled square symbol corresponds to LAE#1, the filled circles to LAE candidates #2 to #7, and the open square to the T-dwarf candidate. Photometric errors are represented by the error bars or arrows depending on whether the objects are detected or not in the  $J$  and/or  $K_s$  bands. Star symbols correspond to L and T-dwarfs (see section 3.3.5). The grey areas correspond to the colors of  $z > 6$  starbursts and  $z < 6$  galaxies with arbitrary reddening values  $E(B - V)$  in the range [0–5] that satisfy the color selection criteria used in this work. The template spectra used to compute the colors are described in Ilbert et al. (2009) and are without emission lines. When adding an emission line to the spectra, the points move to the left of the plot parallel to a line of slope 1. The corresponding lines drawn from the bluest NB1060 –  $K_s$  datapoints at redshifts 0.61 (blue), 1.1 (green) and 1.8 (red) are indicated. Emission line galaxies at these redshifts are located above these lines.

#### 3.3.1. Electronic crosstalk

The WIRCcam detectors suffer from relatively strong electronic cross-talk. The main effect consists in the appearance of ghost images every 32 rows or columns around bright and saturated stars. Three types of electronic ghosts have been identified: positive, negative and ‘edge’ ghosts, the latter consisting of spot images positive on one edge and negative on the other edge. The pattern of these electronic ghosts follows the sky on the images since it is directly associated with (bright) sky objects. Only the positive ghosts are likely to generate false candidates. They are however easily recognizable since they are distributed along columns with a fixed pattern originating from the brightest stars. Median filtering every other 32 detector rows – corresponding to the number of amplifiers – allows one to highlight the ghosts while removing the real objects. This allows one to easily identify most of the ghosts present in the images and to ignore them at the source – this is what was done and most of the ghosts did not contaminate our initial samples of candidates. After careful further investigation, 2 suspicious objects were discarded and accounted for as electronic ghosts for presenting several similarities with the pattern of brighter ghosts.

**Table 2.** Table of the  $z \sim 7.7$  LAE and T-dwarf candidates.

Id.	NB1060	Error	SNR (NB1060)	$J$	Error	$SNR(J)$	$H$	Error	$SNR(H)$	$K_s$	$EW^a$ (Å)
LAE#1	24.0	0.08	14.5	24.5	0.16	6.7	24.7	0.3	4	>24.7	13
LAE#2	24.3	0.17	6.5	>25.0	---	---	>24.7	---	---	>24.7	>16
LAE#3	24.6	0.15	7.2	>25.2	---	---	>24.7	---	---	>24.8	>15
LAE#4	24.8	0.19	5.8	>25.2	---	---	>24.7	---	---	>24.8	>11
LAE#5	24.9	0.2	5.5	>25.2	---	---	>24.7	---	---	>24.8	>9
LAE#6 <sup>b</sup>	25.1	0.19	5.9	>25.0	---	---	>24.7	---	---	>24.7	>5
LAE#7 <sup>b</sup>	25.1	0.22	4.9	>25.0	---	---	>24.7	---	---	>24.7	>5
TDW#1 <sup>c</sup>	24.3	0.12	9.4	24.2	0.15	7.3	>24.7	---	---	>24.7	–

<sup>a</sup> Restframe<sup>b</sup> These two objects are not categorically identified as line emitting objects, but are still probably LAEs, see text<sup>c</sup> This object is not formally part of the sample because it is likely a late type T-dwarf, see text**Fig. 2.** Thumbnail images of all candidates in the final sample listed in table 2. Object TDW#1 is displayed for reference but is not part of the LAE sample (see text). Objects Id's and photometric bands are indicated.

### 3.3.2. Persistence

Another well-known effect of the IR detectors is that pixels illuminated by bright and / or saturated stars in one image continue to release electrons long after the illumination has stopped. This generates fake objects at the positions once illuminated by bright stars previously during the night. These fake sources remain fixed on the detector and therefore do not follow the sky during the dithering pattern. In principle they are removed by sigma clipping or min-max rejection when the images are stacked, however faint residuals may remain. Indeed a pattern of faint objects reproducing the pattern of telescope offsets was observed around the brightest stars in the image, generating false candidates which could be easily removed.

### 3.3.3. Noise

Following the approach from Iye et al. (2006), we have  $\sim 10^6$  1.5'' (diameter) circular apertures in our NB data. Since all of our candidates have  $\text{SNR} \geq 5$ , and assuming a gaussian distribution of the noise, the probability of false  $5\sigma$  events is  $\sim 0.3$ . This is admittedly a crude analysis which does not take into account the fact that the noise properties of the stacked and resampled NB image deviate from a gaussian distribution. If contamination by noise might possibly take place at very low level close to the detection limit, noise certainly cannot be a plausible source of contamination for higher SNR objects.

### 3.3.4. Transient Objects

At the flux limit of the survey, distant supernovae can be visible for several weeks, and therefore be a potential source of contamination.

We computed the expected number of Type Ia and Type II supernovae that would be visible in our narrow-band WIRCam images, by using the same method presented in Cuby et al. (2007). For a limiting magnitude of 24.8 corresponding to one year of data (see table 1), we find that  $\sim 3$  supernovae can be present in the area covered by our data. While contamination by SNe is therefore probable in individual one-year stacks, such objects are automatically removed from our final list of candidates because of the condition that they be present in both 1-yr images. Similarly, stacking of data acquired over long time spans automatically removes point-like slowly moving solar system objects.

### 3.3.5. T-dwarfs

Using the Tinney et al. (2003) spectral type vs. absolute magnitude relations we infer that we could detect T-dwarfs from 300 to 1000 pc, depending on spectral type, from the coolest to the warmest. Considering the high galactic latitude of our field, this extends our sensitivity to T-dwarfs far beyond the Galactic disk scale height. Truncating to a Galactic disk scale height of 350 pc applicable to the population of T-dwarfs (Ryan et al. 2005), we derive a sampled volume of  $\sim 400 \text{ pc}^3$ . Considering a volume density of T-dwarfs of a few  $10^{-3} \text{ pc}^{-3}$ , we expect no more than one T-dwarf in our field. At a couple of hundreds of parsecs from the Sun the proper motion of these objects would not be detected over a one year timescale.

We used the public library of L and T-dwarfs spectra compiled by A. Burgasser (<http://web.mit.edu/ajb/www/tdwarf>) to compute the  $\text{NB1060} - J$  colors expected for these objects. Including T-dwarfs as late as T8 (for which NIRC spectra are

**Table 3.** Extremely Red Objects -  $\text{NB1060}$ ,  $K_s$  magnitudes and size

Id	$\text{NB1060}^a$	Error	$K_s^a$	Error	Size <sup>a</sup>
ERO#1	25.1	0.4	22.5	0.1	3.3
ERO#2	24.2	0.3	23	0.1	1.9
ERO#3	24.2	0.3	22.5	0.15	1.3

<sup>a</sup> MAG\_AUTO as given by SExtractor

<sup>b</sup> FWHM in arcsec in the  $K_s$  band

available), the colours satisfy (see figure 3) :

$$(\text{NB1060} - J)_{\text{T-dwarfs}} > 0 \quad (7)$$

One of the brightest candidates detected in the  $J$  band has  $\text{NB1060} - J$  colors satisfying this criterion and is therefore classified as a late type T-dwarf (TDW#1). The two objects LAE#6 and #7 have  $\text{NB1060} - J$  upper limit values also consistent with late type T-dwarfs. However, because (i) these are only upper limits (ii) we are not expecting many T-dwarfs in our data (see section 3.3.5) and (iii) these two objects are likely to be line emitters (see section 3.2), we assume in the following that only TDW#1 is a T6 to T8 T-dwarf. We show in section 3.3.8 that it could also be, in principle, a high-redshift Lyman Break Galaxy, but this does seem less likely.

### 3.3.6. Extremely Red Objects

The extremely red objects (EROs) are usually defined by their  $R - K$  color, e.g.  $R_{\text{AB}} - K_{\text{AB}} \geq 3.4$ , possibly with additional color criteria (Cimatti et al. 2002), and their fluxes increase towards longer wavelengths. They are generally identified as either passively evolving, old elliptical galaxies, or dusty starburst galaxies (Pierini et al. 2004; Bergström & Wiklind 2004). Despite their faintness in the optical bands, the vast majority of the ERO population present in our data are detected in the  $r'$ ,  $i'$  or  $z'$  bands, and therefore not selected as LAE candidates. In practice, only 3 objects which passed our initial selection criteria were identified as EROs based on their bright red  $\text{NB1060} - K_s$  colors, and the three of them are spatially resolved. Their  $K_s$  magnitudes and sizes are given in table 3. After removal of these 3 objects from our sample, none of the remaining objects are detected in the  $K_s$  band. The  $K_s$  band data, although of limited depth, do therefore provide a reasonably robust selection tool for discriminating EROs from LAE candidates.

### 3.3.7. Low redshift Emitters

As shown in Eq.4 our candidates exhibit a very strong color break of about three magnitudes between the optical part of the spectrum and  $1.06 \mu\text{m}$ . Contamination could occur from peculiar emission line objects such as strong star forming, low metallicity galaxies with an emission line redshifted in the NB filter and an underlying continuum so faint that it would remain undetected in any of the optical broad band filters. The most likely sources of low redshift contamination are from  $\text{H}\alpha$  emitters at  $z = 0.61$ , [OIII] emitters at  $z = 1.1$  and [OII] emitters at  $z = 1.8$ . We first make use of figure 3 to evaluate the  $EW$  of the emission lines required at these redshifts to contaminate our sample. Such emission line galaxies are located above the colored lines, and for their near-IR colors to be consistent with our data (to the extreme left of the plot) would require a contribution of the emission lines to the  $\text{NB1060}$  flux of several magnitudes, equivalent



to restframe equivalent widths of several hundreds or thousands of Angstroms. We now discuss each source of contamination in turn.

#### *H $\alpha$ emitters at $z = 0.61$*

To estimate the number of H $\alpha$  emitters present in our WIRCam image we use the H $\alpha$  luminosity function of Tresse et al. (2002) without reddening correction. To our detection limit, and assuming that the NB flux is dominated by the H $\alpha$  line flux, we derive that we have  $\sim 300$  H $\alpha$  emitters in our filter and field of view in the redshift interval [0.607–0.623]. The vast majority of these emitters are bright in the optical and therefore not selected. Indeed, using the Ilbert et al. (2005) luminosity functions in the restframe UBV filters and in the redshift bin [0.60–0.8] we estimate the limiting magnitude providing 300 objects in the comoving volume sampled by the H $\alpha$  line through the NB1060 filter. We obtain magnitudes of 25.8, 26 and 25.6 corresponding approximately to the  $r'i'z'$  filters at redshift 0.6, i.e. more than 1.5 magnitude below the limiting magnitudes of the CFHT-LS in the  $r'$  and  $i'$  filters. No normal  $z = 0.61$  galaxy spectral energy distribution can therefore contaminate our sample.

In the extreme case of a pure line emission spectrum, the sensitivity limits in the  $r'$  and  $i'$  bands correspond to [OII] and [OIII] flux limits of  $3 \times 10^{-18}$  ergs s $^{-1}$  cm $^{-2}$  and  $2 \times 10^{-18}$  ergs s $^{-1}$  cm $^{-2}$  respectively. Assuming an intrinsic Balmer decrement of 2.8 for case B recombination, this would correspond to [OII]/H $\beta$  and [OIII]/H $\beta$  ratios respectively below 1.0 and 0.71. In the sample of galaxies between redshifts 0.4 and 3 presented in Maier et al. (2006), no objects meet these criteria simultaneously. All objects with low [OIII]/H $\beta$  ratios have strong [OII]/[OIII] ratios, and either of the two [OII] or [OIII] lines should therefore be detected.

In conclusion of this analysis, we argue that contamination by  $z = 0.61$  galaxies is unlikely to bias significantly our sample.

#### *[OIII] emitters at $z = 1.1$*

At redshifts 1.12, similarly to the case above, the vast majority of the [OIII] emitters in the comoving volume sampled by the NB filter will be detected in the optical bands. We use Fig. 13 of Kakazu et al. (2007) to estimate at about 100 the number of [OIII] emitters in our NB image, assuming no dramatic evolution in the [OIII] LF between redshifts 0.83 and 1.1 and considering that the line emission dominates the NB1060 flux. Contamination in our sample could only take place from low luminosity, high  $EW$  [OIII] emitters, unlikely to represent more than a handful of objects. Even so, for [OII] not to be detected in the  $i'$  filter would require a [OIII]/[OII] ratio of 4 or higher at the detection limits of the  $i'$  and NB images. In the data presented in Maier et al. (2006) at redshifts between 0.4 and 3, no more than 5% of the galaxies have such high values. In total, it is therefore unlikely that our sample be contaminated by [OIII] interlopers.

#### *[OII] emitters at $z = 1.8$*

Using the [OII] luminosity function of Rigopoulou et al. (2005) we estimate the number of [OII] emitters in our NB image at  $\sim 300$  objects. The [OIII] and H $\alpha$  lines at redshift 1.84 fall between the atmospheric windows between the  $J$  and  $H$  bands for [OIII] and between the  $H$  and  $Ks$  bands for H $\alpha$ , and therefore do not contribute to the near-IR fluxes in these bands. Using the Kennicutt (1998) relations between the UV continuum and [OII] luminosities we derive a rough estimate of the optical magnitudes expected for [OII] emitters at  $1.06 \mu\text{m}$ . At the flux limit of our data, we get  $m_{\text{opt}}^{\text{AB}} \approx 25.5$ , which is 2 to 3 magnitudes brighter than the limiting magnitude of our optical data. Even with a large scatter around this value, we expect that the vast majority of [OII] emitters should be readily detected in the op-

tical bands. Dusty starbursts may obviously have much fainter optical magnitudes, but such objects would fall in the category of Extremely Red Objects, which, as explained above, can be discarded from their brightness in the  $Ks$  band. Very strong, and unusual [OII]  $EW$  would be required for dusty [OII] emitters to be selected as candidates without being detected in the  $Ks$  band, and such objects would likely be spatially resolved.

We note that Taniguchi et al. (2005) suggest that the few line emitters in their sample of  $z = 6.5$  LAE candidates resisting a definitive identification as LAEs could be [OII] emitters. Some, if not all, of these [OII] emitters would probably be detected in the  $Ks$  band with the same detection limit as ours. We therefore argue that contamination by [OII] emitters in our survey is likely to be low and unlikely to contaminate a large fraction of our sample.

### 3.3.8. High-redshift LBGs

Bright high-redshift Lyman Break Galaxies (LBGs) can be detected in the NB1060 filter through their UV continuum. For this to happen, the redshift shall be smaller than our target value of 7.7, but high enough for these objects to escape detection in the optical images, irrespective of the presence or not of Ly $\alpha$  emission. See Cuby et al. (2003) for such an example.

To estimate the possible contamination by these bright, high- $z$  UV sources, we use the Bouwens et al. (2009) UV LF at  $z \sim 6$  and  $\sim 7$ . As a worst case scenario we consider two redshift ranges: the [6.0–7.0] range for which we use the  $z = 5.9$  UV LF and the range [7.0–7.7] for which we use the  $z = 7.3$  UV LF. I band dropouts may fail detection in the  $z$  band while being detected in the NB1060 filter. While the number of objects is  $\ll 1$  in the second redshift range, it is  $\sim 3$  in the first range. We consider this number as a significantly overestimated number, for the reason that the simple calculation above uses the luminosity function at  $z = 5.9$  which applies to the lower bound of the redshift range and for which the luminosity is brighter. Had we used the  $z = 7.3$  LF to match the [6.0–7.0] range, we would have found 0.2 objects.

We note that these objects would – but for their possible detection in the  $z'$  band – pass all of our selection criteria, but could be mistaken as late type T-dwarfs (see section 3.3.5). Interestingly, one of the brightest candidates in our sample (TDW#1), although primarily thought to be a T-dwarf, could also be a (bright) LBG.

### 3.3.9. Conclusion

We have analyzed various possible sources of contamination for our sample. We note that the magnitudes of our candidates are well distributed, and do not cluster towards the faint end of the luminosity range probed by our survey. This is in itself a sanity check demonstrating that we are not sensitive to a sudden increase of the false alarm rate towards faint fluxes. We note that we have made use of very robust selection criteria to select our candidates, consisting of very strong color breaks between the optical and the near-IR ( $\sim 3$  magnitudes), and rejecting EROs from their bright fluxes in the  $Ks$  band. We argue that our selection criteria are comparable to the criteria used in other LAE or LBG studies and we are therefore confident in the reliability of our sample. We however cannot completely rule out contamination by one or the other sources identified above, in particular artifacts and / or [OII] emitters. In the following, we will evalu-



ate the impact of partial contamination of our sample, at the level of a couple of objects.

## 4. Discussion

### 4.1. Variance

The variance on the number of objects in our sample is due to Poisson errors and to fluctuations in the large scale distribution of galaxies. Various models exist in the literature to account for the effects of cosmic variance. Trenti & Stiavelli (2008) have developed a model which is offered as an on-line ‘cosmic variance calculator’. Assuming a one-to-one correspondence between dark halos and LAEs, we obtain from this model a value of  $\sim 28\%$  for the cosmic variance in our data.

This result however strongly depends on the assumptions used for the level of completeness and contamination factor in our sample. In view of the limited number of objects in our sample and of the large comoving volume ( $\sim 6.3 \times 10^4 \text{ Mpc}^3$ ), our results are probably limited by Poisson noise –  $\sim 38\%$  for 7 objects – more than by clustering variance. We note however that variance due to clumpy re-ionization is ignored and may also contribute to the total variance.

### 4.2. On the Ly $\alpha$ Luminosity function at $z = 7.7$

From our data we can derive constraints on the Ly $\alpha$  luminosity function of  $z = 7.7$  LAEs. We first apply a corrective factor when converting the NB1060 magnitudes to Ly $\alpha$  fluxes. From the  $J$  magnitude of object LAE#1 we infer that the Ly $\alpha$  line contributes to  $\sim 70\%$  of the NB1060 flux, a value similar to the average value observed for the  $z = 6.5$  LAEs of Taniguchi et al. (2005) and which corresponds to an  $EW_{obs}$  of  $\sim 110 \text{ \AA}$  in the observed frame. We adopt this line to continuum ratio in the following to derive the Ly $\alpha$  fluxes from the NB1060 magnitudes, adding a 0.1 magnitude rms error to account for the dispersion of this ratio between objects, consistent with the dispersion of the EW values of Taniguchi et al. (2005). Clearly, deeper  $J$  band imaging or spectroscopy would be required to estimate this fraction on a case by case basis for each object.

To discuss the Ly $\alpha$  luminosity function derived from our sample we first fit a Schechter function  $\Phi(L)$  to our data, where  $\Phi(L)$  is given by:

$$\Phi(L)dL = \Phi^* \left(\frac{L}{L^*}\right)^\alpha \exp\left(-\frac{L}{L^*}\right) \frac{dL}{L^*} \quad (8)$$

Considering the scarcity of datapoints in our sample, we do not attempt at fitting the 3 parameters of the Schechter function. Following typical values adopted by Ouchi et al. (2008) and Kashikawa et al. (2006) for the faint end slope  $\alpha$  of the luminosity function, we use  $\alpha = -1.5$  and derive  $\Phi^*$  and  $L^*$  by a simple  $\chi^2$  minimization. We note that there may be other functions more representative of the Ly $\alpha$  LAE LF at high redshifts. For instance, Kobayashi et al. (2007) derive numerical LFs from models of hierarchical galaxy formation and of the escape fraction of Ly $\alpha$  photons from host galaxies. These LFs differ significantly from a Schechter function. However, for the sake of comparison with previous work, we keep the analytical Schechter formalism.

We initially assume that all of the 7 candidates of the *full* sample are true  $z = 7.7$  LAEs, and derive the corresponding LF parameters. To evaluate the impact of sample contamination on the results, we then consider situations where only 4 candidates among the 7 of the sample are real. As shown earlier in

**Table 4.** Best fit Schechter LF parameters for  $\alpha = -1.5$

Redshift	$\log(L^*(\text{erg s}^{-1}))$	$\log(\Phi^*(\text{Mpc}^{-3}))$
7.7 <sup>a</sup>	43.0 <sup>+0.2</sup> <sub>-0.3</sub>	-3.9 <sup>+0.5</sup> <sub>-0.3</sub>
7.7 <sup>b</sup>	43.3 <sup>+0.6</sup> <sub>-0.6</sub>	-4.4 <sup>+1.2</sup> <sub>-0.7</sub>
7.7 <sup>c</sup>	42.9 <sup>+0.5</sup> <sub>-0.7</sub>	-3.8 <sup>+2.1</sup> <sub>-0.8</sub>
7.7 <sup>d</sup>	42.5 <sup>+0.5</sup> <sub>-0.7</sub>	-3.0 <sup>+3.5</sup> <sub>-1.2</sub>
6.5 <sup>(1)</sup>	42.6 <sup>+0.12</sup> <sub>-0.1</sub>	-2.88 <sup>+0.24</sup> <sub>-0.26</sub>
5.7 <sup>(2)</sup>	42.8 <sup>+0.16</sup> <sub>-0.16</sub>	-3.11 <sup>+0.29</sup> <sub>-0.31</sub>

<sup>a</sup> Full sample of 7 candidates

<sup>b</sup> Mean of the 20 *bright* samples of 4 objects among 7

<sup>c</sup> Mean of the 10 *intermediate* samples of 4 objects among 7

<sup>d</sup> Mean of the 5 *faint* samples of 4 objects among 7, see text References. (1) Kashikawa et al. (2006); (2) Ouchi et al. (2008)

this paper, despite the robustness of our sample, we cannot completely rule out contamination by an instrumental artifact or a low redshift peculiar object. We therefore conjecture that at least 4 objects in our sample must be real  $z = 7.7$  LAEs, and evaluate the impact on the Luminosity Function parameters with such reduced samples. To do this, we consider all combinations of 4 objects from among the 7 in the sample, and compute for each subset the best fit parameters using a Schechter function. The results of the fits for the full sample and for the 35 sub-samples are shown on figure 4, which shows that the fits of the 35 sub-samples of 4 objects naturally divide into 3 different categories:

- a *bright* category of 20 samples which all contain the brightest object (LAE#1)
- an *intermediate* category of 10 samples which do not contain the brightest object but which do contain the second brightest object (LAE#2)
- a *faint* category of 5 samples containing none of the two brightest objects

For each sample we derive the best fit Schechter LF parameters for  $\alpha = -1.5$  and we derive the average parameters, reported in table 4, for each of the three categories defined above. The corresponding average LFs for each category are shown as dashed lines on figure 4. We note that the *full* sample LF (plain black line) corresponds very closely to the LF of the sample of the four brightest objects from the *bright* category. We also note that by removing three objects from the *full* sample while keeping the brightest in the *bright* category, we artificially enhance the  $L^*$  parameter, or alternatively reduce the  $\Phi^*$  parameter of this category. In consequence the *full* sample LF is probably more representative of the situation where the brightest object is real than the average LF of the *bright* category.

To further illustrate our results in the light of the LAE LF at lower redshifts, we plot in figure 5 the error contours for the *full* sample and the *faint* category together with the  $z = 6.5$  and  $z = 5.7$  LFs from Kashikawa et al. (2006) and Ouchi et al. (2008). The errors for the *faint* category are dominated by the fitting errors for each of the five LFs in the category, and to account for the dispersion between samples we simply add to the fitting errors the deviation between the two most extreme LFs in the sample. The *full* sample LF would indicate an evolution between  $z = 7.7$  and  $z = 6.5$  opposite (in  $L^*$  and  $\Phi^*$ ) to the evolution between  $z = 6.5$  and  $z = 5.7$  at the  $2\sigma$  confidence level. Conversely, the *faint* category LF would be consistent with this evolution and with the  $z = 6.96$  datapoint of Iye et al. (2006). In other words, for our data to be consistent with other work requires that both of our brightest objects are not real LAEs.

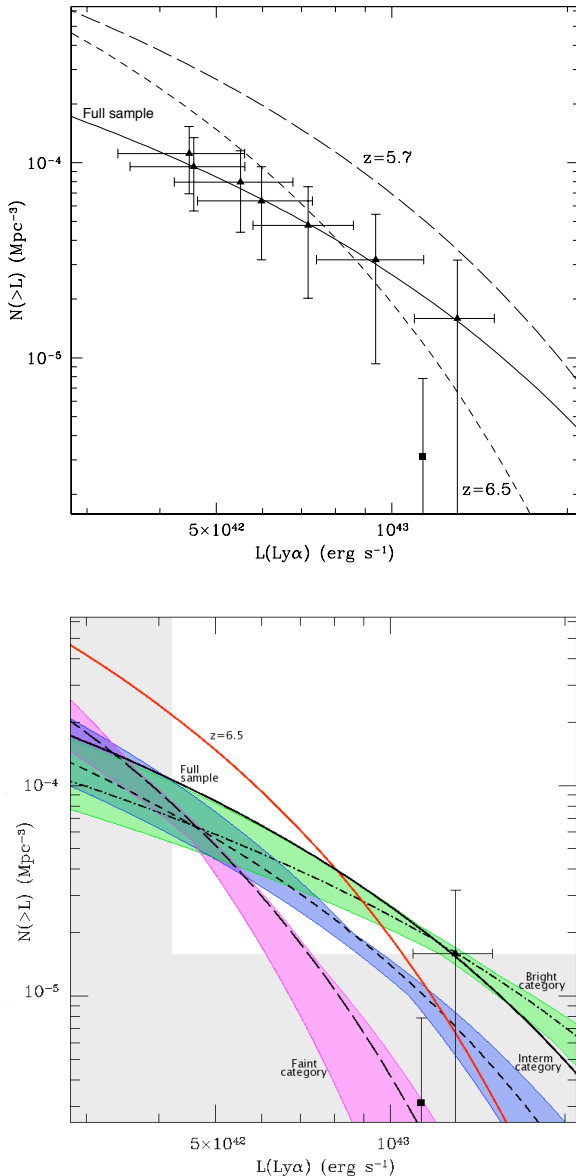


**Fig. 4.** Cumulative Luminosity Functions (LFs) with  $\alpha = -1.5$ . *Up:* Luminosity function derived from the *full* sample. The data (triangles) are not corrected for completeness and a factor of 70% has been used to convert the NB1060 fluxes into Ly $\alpha$  fluxes. The plain line is the best fit Schechter function through the datapoints. The  $z = 5.7$  (Ouchi et al. (2008), long dashed line) and the  $z = 6.5$  (Kashikawa et al. (2006), short dashed line) LFs are also indicated. Each point in the sample and its aperture photometric errors, augmented by the photometric calibration errors and dispersion of the conversion from NB1060 magnitudes to Ly $\alpha$  line fluxes, define the luminosity bins and the horizontal error bars. The vertical error bars represent the Poisson noise associated to the number of candidates. The square point corresponds to the  $z = 6.96$  LAE of Iye et al. (2006). *Bottom:* The shaded color areas represent the range of LFs in each of the three categories described in the text, and the dashed lines represent the associated average LFs. *Bright* category: green area and dot-dashed line; *intermediate* category: blue area and short-dashed line; *faint* category: magenta area and long-dashed line. Also plotted is the LF at  $z = 6.5$  (Kashikawa et al. (2006), plain red line) and the *full* sample  $z = 7.7$  LF (this work, plain black line). The square point is the  $z = 6.96$  LAE of Iye et al. (2006) and the triangle is LAE#1 (this work). The shaded grey areas to the bottom and left of the figure represent the regions where the  $z = 7.7$  LF would lie if none of our candidates were real LAEs.

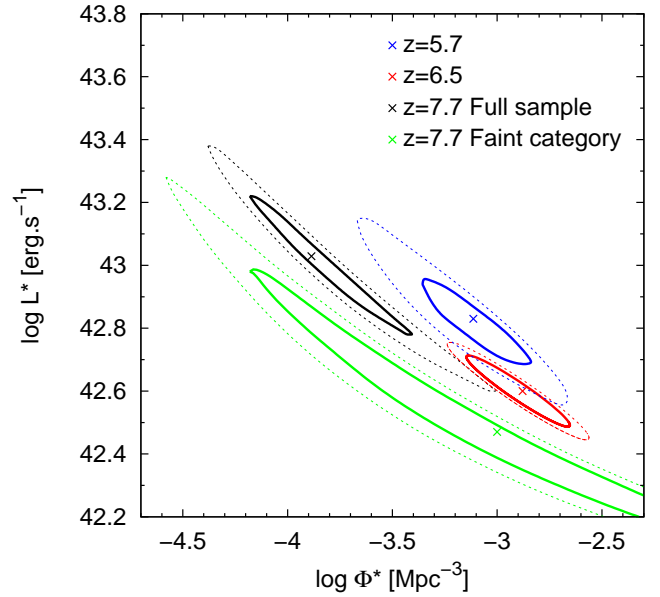


**Fig. 5.** Error ellipses for the best-fit Schechter parameters  $\Phi^*$  and  $L^*$  for  $\alpha = -1.5$ . The solid and dotted line ellipses are respectively the 68% and 95% confidence levels. Are shown the error contours of the Schechter parameters for the *full* sample (black), the *faint* category (green), the  $z = 6.5$  LF (Kashikawa et al. 2006) (red) and the  $z = 5.7$  LF (Ouchi et al. 2008) (blue).

Only spectroscopic confirmation will allow to draw firmer conclusions, which will still be based on small numbers and therefore subject to large uncertainties. Finally, we note that the analysis performed in this section would remain qualitatively and quantitatively similar had we assumed that only 3 of our candidates were real instead of 4.

#### 4.3. Implications

We used the model from Kobayashi et al. (2007) to estimate the ionization fraction of the IGM at  $z = 7.7$  from our constraints on the Ly $\alpha$  LAE LF. This model produces LFs for different values of the IGM transmission to Ly $\alpha$  photons ( $T_{\text{Ly}\alpha}^{\text{IGM}}$ ) used as a global parameter. The Ly $\alpha$  attenuation by the IGM is a complex process originating in the damping wings of the Ly $\alpha$  line and involving the neutral fraction of hydrogen  $x_{\text{HI}}$  and dynamical models of the local IGM infall towards the LAEs (Santos 2004; Dijkstra et al. 2007). Within this model the conversion factor from  $T_{\text{Ly}\alpha}^{\text{IGM}}$  to  $x_{\text{HI}}$  is therefore highly sensitive to the local IGM density and velocity, and may not be representative of the *average* IGM situation. Using this model, to best fit our LFs within the range of observed luminosities, we derive  $T_{\text{Ly}\alpha}^{\text{IGM}}$  values ranging from  $\sim 0.7$  for the *faint* category to 1.0 for the *full* sample.  $T_{\text{Ly}\alpha}^{\text{IGM}} \sim 0.7$  corresponds to  $x_{\text{HI}} \sim 0.3$  in the model of Santos (2004) for a given redshift of the Ly $\alpha$  line with respect to the systemic velocity of the galaxy. This  $x_{\text{HI}}$  value is approximately similar to the one derived from the LAE Ly $\alpha$  LF at  $z = 6.5$  (Kobayashi et al. 2007).

Considering the high level of uncertainty on the  $z = 7.7$  LF derived from our results and on the re-ionization models, we simply note here, in parallel to our earlier conclusions on the LF, that if one or both of our brightest objects is real, a low fraction of neutral hydrogen is inferred ( $\approx 0$ ), in contradiction with

earlier reports of an increasing fraction above  $z \sim 6$ . Even if both of the brightest objects are not real but if a reasonable fraction of the faint objects is real (our faint category), the Kobayashi et al. (2007) model infers a still moderate neutral fraction of hydrogen.

Finally we note that many other models are available in the literature which predict the evolution of the LF of high- $z$  LAEs (Baugh et al. 2005; Le Delliou et al. 2006; Cole et al. 2000; Mao et al. 2007; Thommes & Meisenheimer 2005; Mesinger & Furlanetto 2008), see also Nilsson et al. (2007) for a comparison of some of these models. These models do use various ingredients into the simulations, and discussing our results in the light of each of these models is beyond the scope of this paper. For the sake of visual comparison, we plot in figure 6 our results corresponding to the extreme *full* sample and *faint* category compared to some of these models.

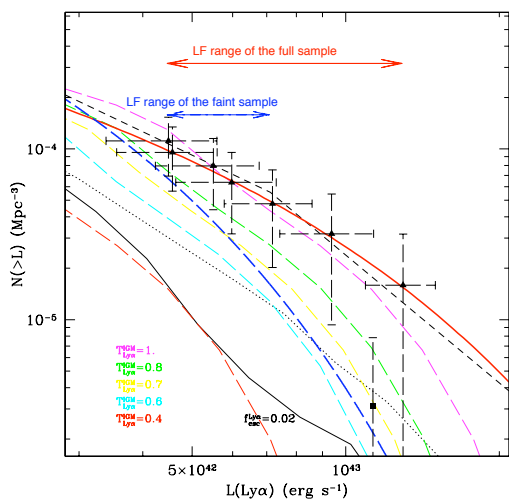


**Fig. 6.** Cumulative Luminosity Functions corresponding to our *full* sample (plain red thick line) and *faint* category (long blue dashed thick line). The range of luminosities sampled by the data for both samples are indicated by the arrows. Thin lines are  $z \sim 8$  LFs from various models: Baugh et al. (2005) (plain line), Mao et al. (2007) (dotted line), Thommes & Meisenheimer (2005) (short-dashed line), Kobayashi et al. (2007) (color long-dashed lines for various IGM Ly $\alpha$  transmissions  $T_{Ly\alpha}^{IGM}$ ) as indicated. The square point is the  $z = 6.96$  LAE of Iye et al. (2006)

## 5. Conclusions

We have searched  $z = 7.7$  LAEs in a deep narrow-band image at  $1.06 \mu\text{m}$  obtained with WIRCam at CFHT, totalling 40 hrs of integration time and covering  $390 \text{ arcmin}^2$  and sampling a comoving volume of  $6.3 \times 10^4 \text{ Mpc}^3$ , down to a limit in Ly $\alpha$  luminosity of  $8.3 \times 10^{-18} \text{ ergs s}^{-1} \text{ cm}^{-2}$ .

Using deep visible data of the field, we have selected LAE candidates presenting a strong color break of up to 3 magnitudes between the visible data and the NB1060 filter. We have obtained a sample of seven carefully selected candidates. We have analyzed all sources of contamination that we could think of, and argued that contamination is unlikely to affect all of our candidates.

We found that the Ly $\alpha$  LAE luminosity functions derived from our photometric sample, within the limitations of the

Schechter formalism and with a fixed slope parameter  $\alpha = -1.5$ , would contradict the evolution in luminosity found by Kashikawa et al. (2006) between  $z = 5.7$  and  $z = 6.5$  at the  $1\sigma$  to  $2\sigma$  confidence level if only one of our two brightest objects is real. Only spectroscopic follow-up of objects in our sample will allow to derive firmer conclusions.

Using models of Ly $\alpha$  LAE LFs available in the literature, and contingent upon their reliability, we infer from our results that the fraction of neutral hydrogen at  $z = 7.7$  should be in the range  $[0.0 - 0.3]$ .

*Acknowledgements.* The authors would like to thank the anonymous referee for constructive comments which helped us to improve the precision and clarity of the paper ; R. Ellis for granting us observing time at the Keck Observatory to attempt spectroscopy on an early candidate (which later turned out to be detected on the latest CFHTLS release) and J. Richard for performing these Keck observations ; J.Mao, A.Lapi, C.Baugh, A.Orsi, M. Kobayashi, E.Thommes, for providing their model data and M.Trenti and T.Totani for helpful discussions. We acknowledge support from the French Agence Nationale de la Recherche, grant number ANR-07-BLAN-0228.

## References

- Baugh, C. M., Lacey, C. G., Frenk, C. S., et al. 2005, MNRAS, 356, 1191  
 Bergström, S. & Wiklind, T. 2004, A&A, 414, 95  
 Bertin, E. & Arnouts, S. 1996, A&AS, 117, 393  
 Bouwens, R. J., Illingworth, G. D., Bradley, L. D., et al. 2009, ApJ, 690, 1764  
 Bouwens, R. J., Illingworth, G. D., Franx, M., & Ford, H. 2008, ApJ, 686, 230  
 Cimatti, A., Daddi, E., Mignoli, M., et al. 2002, A&A, 381, L68  
 Cole, S., Lacey, C. G., Baugh, C. M., & Frenk, C. S. 2000, MNRAS, 319, 168  
 Coupon, J., Ilbert, O., Kilbinger, M., et al. 2008, ArXiv e-prints  
 Cuby, J.-G., Hiben, P., Lidman, C., et al. 2007, A&A, 461, 911  
 Cuby, J.-G., Le Fèvre, O., McCracken, H., et al. 2003, A&A, 405, L19  
 Dijkstra, M., Lidz, A., & Wyithe, J. S. B. 2007, MNRAS, 377, 1175  
 Fan, X., Carilli, C. L., & Keating, B. 2006, ARA&A, 44, 415  
 Ilbert, O., Arnouts, S., McCracken, H. J., et al. 2006, A&A, 457, 841  
 Ilbert, O., Capak, P., Salvato, M., et al. 2009, ApJ, 690, 1236  
 Ilbert, O., Tresse, L., Zucca, E., et al. 2005, A&A, 439, 863  
 Iovino, A., McCracken, H. J., Garilli, B., et al. 2005, A&A, 442, 423  
 Iye, M., Ota, K., Kashikawa, N., et al. 2006, Nature, 443, 186  
 Kakazu, Y., Cowie, L. L., & Hu, E. M. 2007, ApJ, 668, 853  
 Kashikawa, N., Shimasaku, K., Malkan, M. A., et al. 2006, ApJ, 648, 7  
 Kennicutt, Jr., R. C. 1998, ARA&A, 36, 189  
 Kobayashi, M. A. R., Totani, T., & Nagashima, M. 2007, ApJ, 670, 919  
 Lawrence, A., Warren, S. J., Almaini, O., et al. 2007, MNRAS, 379, 1599  
 Le Delliou, M., Lacey, C. G., Baugh, C. M., & Morris, S. L. 2006, MNRAS, 365, 712  
 Lonsdale, C. J., Smith, H. E., Rowan-Robinson, M., et al. 2003, PASP, 115, 897  
 Maier, C., Lilly, S. J., Carollo, C. M., et al. 2006, ApJ, 639, 858  
 Mao, J., Lapi, A., Granato, G. L., de Zotti, G., & Danese, L. 2007, ApJ, 667, 655  
 Marigo, P., Girardi, L., Bressan, A., et al. 2008, A&A, 482, 883  
 Marmo, C. 2007, in Astronomical Society of the Pacific Conference Series, Vol. 376, Astronomical Data Analysis Software and Systems XVI, ed. R. A. Shaw, F. Hill, & D. J. Bell, 285–+  
 Mesinger, A. & Furlanetto, S. R. 2008, MNRAS, 386, 1990  
 Nilsson, K. K., Orsi, A., Lacey, C. G., Baugh, C. M., & Thommes, E. 2007, A&A, 474, 385  
 Ota, K., Kashikawa, N., Malkan, M. A., et al. 2008, ArXiv e-prints, 804  
 Ouchi, M., Shimasaku, K., Akiyama, M., et al. 2008, ApJS, 176, 301  
 Pickles, A. J. 1998, PASP, 110, 863  
 Pierini, D., Gordon, K. D., Witt, A. N., & Madsen, G. J. 2004, ApJ, 617, 1022  
 Richard, J., Pelló, R., Schaerer, D., Le Borgne, J.-F., & Kneib, J.-P. 2006, A&A, 456, 861  
 Richard, J., Stark, D. P., Ellis, R. S., et al. 2008, ApJ, 685, 705  
 Rigopoulou, D., Vacca, W. D., Berta, S., Franceschini, A., & Aussel, H. 2005, A&A, 440, 61  
 Ryan, Jr., R. E., Hathi, N. P., Cohen, S. H., & Windhorst, R. A. 2005, ApJ, 631, L159  
 Santos, M. R. 2004, MNRAS, 349, 1137  
 Stark, D. P., Ellis, R. S., Richard, J., et al. 2007, ApJ, 663, 10  
 Taniguchi, Y., Ajiki, M., Nagao, T., et al. 2005, PASJ, 57, 165  
 Thommes, E. & Meisenheimer, K. 2005, A&A, 430, 877  
 Tinney, C. G., Burgasser, A. J., & Kirkpatrick, J. D. 2003, AJ, 126, 975  
 Trenti, M. & Stiavelli, M. 2008, ApJ, 676, 767  
 Tresse, L., Maddox, S. J., Le Fèvre, O., & Cuby, J.-G. 2002, MNRAS, 337, 369

Willis, J. P. & Courbin, F. 2005, MNRAS, 357, 1348

Willis, J. P., Courbin, F., Kneib, J.-P., & Minniti, D. 2008, MNRAS, 384, 1039